Journal of Materiomics 6 (2020) 274–279

Contents lists available at ScienceDirect

Journal of Materiomics

journal homepage: www.journals.elsevier.com/journal-of-materiomics/

Effect of group-3 elements doping on promotion of in-plane Seebeck coefficient of n-type Mg_3Sb_2

Chengliang Xia [a], Juan Cui [a], Yue Chen [a, b, *]

[a] Department of Mechanical Engineering, The University of Hong Kong, Pokfulam Road, Hong Kong SAR, China
[b] HKU Zhejiang Institute of Research and Innovation, 1623 Dayuan Road, Lin An, 311305, China

ARTICLE INFO

Article history:
Received 6 January 2020
Received in revised form
17 February 2020
Accepted 3 March 2020
Available online 7 March 2020

Keywords:
Thermoelectric materials
Mg_3Sb_2-based alloys
group-3 elements
n-type dopants

ABSTRACT

Mg_3Sb_2-based alloys are promising thermoelectric materials with a reasonably low thermal conductivity. However, their electrical transport property is usually limited by the low carrier concentration. Mg_3Sb_2 has a multi-valley conduction band with a six-fold degeneracy, benefiting n-type thermoelectric performance. Recently, n-type Y-doped $Mg_3Sb_{1.5}Bi_{0.5}$ and Sc-doped Mg_3Sb_2–Mg_3Bi_2 alloys show a large figure of merit (ZT). In this paper, the doping effect of group-3 and chalcogen elements on the electronic structures and electrical transport properties of Mg_3Sb_2 was investigated *via* the first-principles calculations. Chalcogen elements have a slight effect on the electronic structure, and Te-doped Mg_3Sb_2 shows better normalized power factors in both the out-of-plane and in-plane directions, compared to the S-doped and Se-doped systems. Distinctly different doping effects appear in Mg_3Sb_2 doped with group-3 elements. A increased density of states near the bottom of the conduction band can be induced by Sc or Y. Sc-doped and Y-doped Mg_3Sb_2 show higher normalized power factors along the in-plane direction than those doped with chalcogens.

1. Introduction

Thermoelectric materials have attracted much research interest because they can transform heat to electrical power or vice versa [1]. These materials are applied in narrow fields, such as green power generation and electronic industry [2,3]. Since most commercial thermoelectric materials, such as Bi_2Te_3 or PbTe, are based on rare or toxic elements, some alternative materials need to be explored [4].

Bredt and Kendall firstly reported that Mg_3Sb_2 is a potential thermoelectric material [5,6]. Mg_3Sb_2 is a semiconductor with a small band gap of 0.8 eV [7], and it has intense alloying ability and structural stability [8,9]. Mg_3Sb_2 has a reasonably low thermal conductivity, which is beneficial to the thermoelectric performance. It also has other advantages, such as, low mass density and low vapor pressure [6]. However, the poor electrical transport properties and the low carrier concentration (10^{17} cm^{-3}) of pristine Mg_3Sb_2 restrict its thermoelectric efficiency [10,11]. Condron et al. found that Mg_3Sb_2 degrades at > 900 K and the maximum thermoelectric figure of merit (ZT) is 0.21 at 875 K [6].

Pristine Mg_3Sb_2 is intrinsically p-type, and other p-type Mg_3Sb_2-based materials are also investigated extensively, such as Ag-doped and Na-doped Mg_3Sb_2 [12–14]. Song et al. reported that the ZT of p-type $Mg_{2.985}Ag_{0.015}Sb_2$ reaches 0.51 at 725 K [13]. It is difficult to synthesize N-type Mg_3Sb_2-based materials due to the formation of Mg vacancies. In recent years, n-type Mg_3Sb_2-based materials with promising thermoelectric efficiencies are obtained by introducing Sb/Bi disorder and effective dopants, such as Mn and Te [7,11,15–17]. The figure of merit (ZT) of Te-doped $Mg_3Sb_{1.5}Bi_{0.5}$ at 300 K is 0.56, and it increases to 1.65 at 725 K. It was proposed that the improved thermoelectric performance of n-type $Mg_3Sb_{1.5}Bi_{0.5}$ is due to the multi-valley conduction band with a six-fold degeneracy and a light carrier effective mass.

Recent studies demonstrated that Y and Sc are effective n-type dopants in Mg_3Sb_2 [18–20]. These dopants are found to increase the carrier concentration and enhance the carrier mobility of Mg_3Sb_2 compound. Y-doped $Mg_3Sb_{1.5}Bi_{0.5}$ and Sc-doped Mg_3Sb_2–Mg_3Bi_2 alloys both achieve a relatively high ZT value of 1.1 at 300-500 K. In addition, theoretically achievable carrier

* Corresponding author. Department of Mechanical Engineering, The University of Hong Kong, Pokfulam Road, Hong Kong SAR, China.
E-mail address: yuechen@hku.hk (Y. Chen).
Peer review under responsibility of The Chinese Ceramic Society.

https://doi.org/10.1016/j.jmat.2020.03.003

concentrations of group-3 elements in Mg_3Sb_2 were also reported [21,22]. Nonetheless, the effects of Y and Sc on the electronic structure and electrical transport properties of Mg_3Sb_2 are further investigated yet.

The thermoelectric energy conversion efficiency is described by the dimensionless figure of merit ZT, which is defined by

$$ZT = \frac{\sigma S^2}{\kappa} T \quad (1)$$

where σ is the electrical conductivity, S is the Seebeck coefficient, and κ is the thermal conductivity. High power factor and low thermal conductivity are required to achieve high-performance thermoelectric materials. Band engineering [23–26], e.g., the induction of resonant states and the increase of band convergence, is effective in enhancing the power factor and the thermoelectric figure of merit ZT. In this paper, we focus on a study on potential n-type dopants and their effects on the electronic structure and electrical transport properties since n-type Mg_3Sb_2 has a higher thermoelectric efficiency,

2. Computational details

Density functional theory (DFT) [27,28] calculations were performed using the Vienna ab-initio simulation package (VASP) [29,30]. Effective band structures were computed by unfolding the electronic bands with BandUP [31]. Generalized gradient approximation (GGA) in the form of Perdew-Burke-Ernzerhof (PBE) parametrization was employed [32]. The TB-mBJ potential was also considered to correct the band gap [33]. The calculations of the electrical transport properties were performed based on the Boltzmann transport theory as implemented in BoltzTraP2 [34]. The constant relaxation time approximation was employed to investigate the electrical transport properties of doped Mg_3Sb_2 systems.

We set an energy cutoff of 600 eV in the DFT calculations. Relaxation and charge self-consistent calculations were converged to 10^{-6} eV. Cell and internal atomic coordinates both were fully relaxed until the force component was smaller than 10 meV/Å. The Brillouin zone was meshed with a density of $2\pi \times 0.02$ Å^{-1}, using Γ-centered Monkhorst-Pack grids. A denser *k*-point mesh of about $2\pi \times 0.01$ Å^{-1} was used to calculate the electrical transport properties. A 2×2×2 supercell containing 40 atoms, based on the Mg_3Sb_2 $P\bar{3}m1$ primitive cell, was constructed with one Mg or Sb atom substituted by one doping atom. For effective band structure calculations, atomic positions were relaxed after doping while the supercell vectors were fixed. For other calculations, supercells were fully optimized. The decomposed charge density of n-type Mg_3Sb_2 was calculated by summing conduction electrons of all bands from the conduction band minimum to the energy level that corresponds to a carrier concentration of -10^{20} cm^{-3}. A larger supercell containing 90 atoms was used to verify the reliability of the results, as shown in Figs. S2 and S5 in the Supplemental Material.

Quantum Espresso [35] and EPW [36] were used to calculate the electronic relaxation time of Mg_3Sb_2 based on DFT and density functional perturbation theory (DFPT). The electronic relaxation time was used in the calculation of the electrical transport properties of Mg_3Sb_2 with BoltzTraP2 [34]. Norm-conserving relativistic pseudopotentials [37,38] were applied. A kinetic energy cutoff of 80 Ry and a 14×14×8 *k*-mesh were used in the self-consistent calculations. The crystal structure was fully relaxed until the total energy was converged to 10^{-6} Ry and the atomic forces were smaller than 10^{-5} Ry/a.u. Phonons were calculated with a 7×7×4 *q*-mesh. For the electron-phonon matrix element calculations, the 14×14×8 *k*-mesh and 7×7×4 *q*-mesh were interpolated to 70×70×40 fine *k*-mesh and 35×35×20 fine *q*-mesh, respectively. The results calculated with different fine *k*-mesh and *q*-mesh are shown in Fig. S3 in Supplemental Material. A scissor shift was applied to correct the band gap to the experimental value of 0.8 eV [7].

3. Results and discussion

Fig. 1**a)** shows the trigonal crystal structure of Mg_3Sb_2, which has a space group of $P\bar{3}m1$. Mg_3Sb_2 is generally regarded as a Mg^{2+} layer and a covalently bonded $[Mg_2Sb_2]^{2-}$ layer. There are three Wyckoff positions in Mg_3Sb_2, two Mg sites and one Sb site, and these positions are denoted in Fig. 1**a)**. Mg1 and Mg2 represent Mg atoms in Mg^{2+} layer and $[Mg_2Sb_2]^{2-}$ layer, respectively. The interstitial site (0, 0, 1/2) in Mg_3Sb_2 lattice is also noted. Fig. 1**b)** and Fig. 1**c)** show the density of states and the band structure of pristine Mg_3Sb_2 calculated with TB-mBJ potential. The theoretical band gap of Mg_3Sb_2 is 0.65 eV, which is in reasonable agreement with the experimental band gap (0.8 eV) [7]. The valence band maximum locates at Γ point, and the conduction band minimum (CBM) locates in the path from M*(0, 0.417,0) to L*(0, 0.417, 0.5). Zhang et al. demonstrated that the multi-valley band with a six-fold degeneracy along M*-L* and a duple valley conduction band at the K point promote the thermoelectric efficiency of n-type Mg_3Sb_2 [11]. Fig. 1**d)** shows the electron-phonon scattering rate of Mg_3Sb_2 near the band edges at 300 K and 600 K. The electronic relaxation time is calculated from the imaginary part of the electron self-energy. The scattering rate is the inverse of the electronic relaxation time [36].

$$\frac{1}{\tau_{nk}} = 2\Sigma''_{nk}(\omega, T) \quad (2)$$

where τ_{nk} is the electronic relaxation time of band *n* at wavevector *k*; $\Sigma''_{nk}(\omega, T)$ denotes the imaginary part of the electron self-energy. It is seen that the scattering rates of the electronic states close to the band edges are smaller, indicating weaker electron-phonon interactions. Electrons that are further away from the band gap can be more easily scattered to their final states [39].

The Seebeck coefficient, the electrical conductivity, and the power factor of Mg_3Sb_2 are calculated using EPW and BoltzTraP2, as shown in Fig. 2. Clearly, the power factor of n-type Mg_3Sb_2 (negative carrier density) is generally larger than that of p-type Mg_3Sb_2 (positive carrier density), indicating that n-type Mg_3Sb_2 may exhibit a higher thermoelectric performance. Therefore, the calculations are consistent with previous experimental findings [11,16]. The calculated *S* and σ are, respectively, 2–3 times smaller and 4–6 times larger than the experimental data [13,40,41], being similar to previous electrical transport calculations of GeTe [39]. A difference between the theoretical and experimental results could be related to the defects in real materials.

Doping can be effective in improving the thermoelectric performance of Mg_3Sb_2 [9,21,43]. In this work, the effect of group-3 (i.e., Sc and Y) and chalcogen group elements (i.e., S, Se and Te) doping are systematically investigated. It was found that group-3 elements (i.e., Sc and Y) tend to occupy the Mg1 lattice site, while the chalcogen group elements (i.e., S, Se and Te) tend to occupy the Sb lattice site [21,22]. Therefore, these doped Mg_3Sb_2 systems are expected to be n-type because the doping atoms tend to donate one extra electron rather than the substituted atoms.

The density of states of doped and pristine Mg_3Sb_2 was calculated to investiagte the electronic structure changes. The conduction band minimum shifts to zero for direct comparison. Since the optimal carrier concentration of most thermoelectric materials is usually in the range of 10^{19}–10^{21} cm^{-3}, the energy levels corresponding to a carrier density of -10^{20} cm^{-3} are shown in Fig. 3**a)**. It is seen that the DOS of Sc-doped and Y-doped Mg_3Sb_2 largely

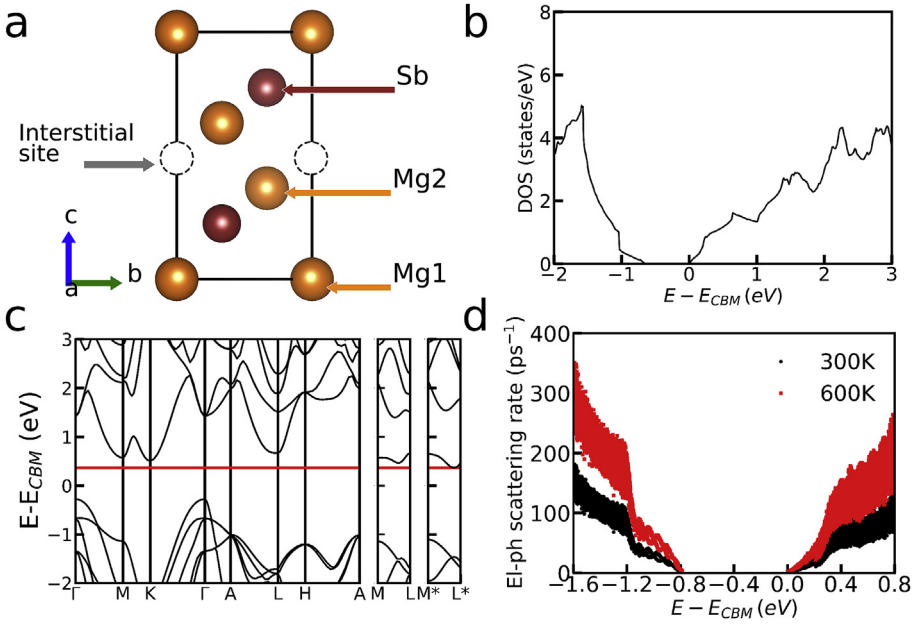

Fig. 1. a) Lattice structure of Mg_3Sb_2; the three Wyckoff positions and the interstitial site are denoted. **b)** Electronic density of states and **c)** band structure of pristine Mg_3Sb_2 calculated with TB-mBJ potential. **d)** Electron-phonon scattering rate of Mg_3Sb_2 with respect to the conduction band minimum at 300 K (black dots) and 600 K (red dots).

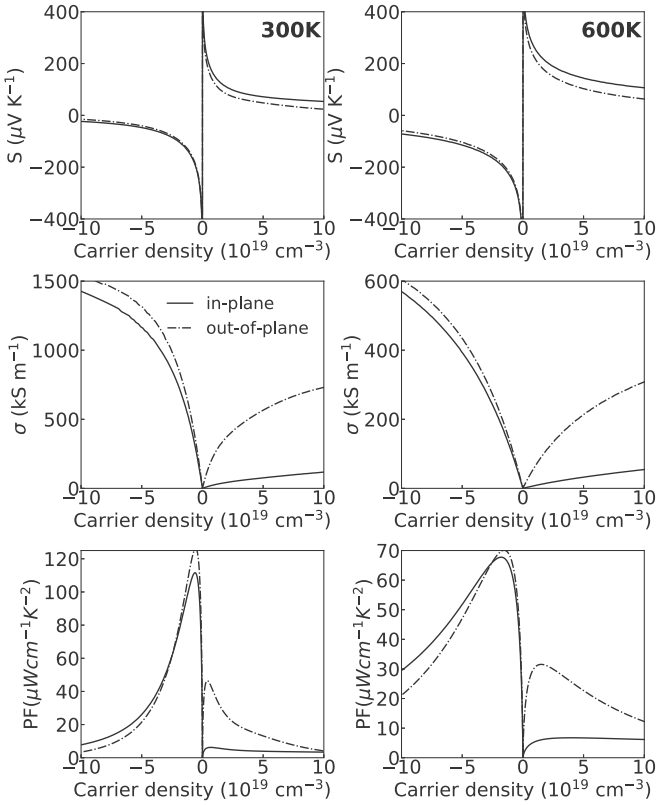

Fig. 2. The Seebeck coefficients (top), electrical conductivities (middle), and power factors (bottom) of Mg_3Sb_2 at 300 K and 600 K. Hole and electron carrier concentrations are represented by positive and negative values, respectively.

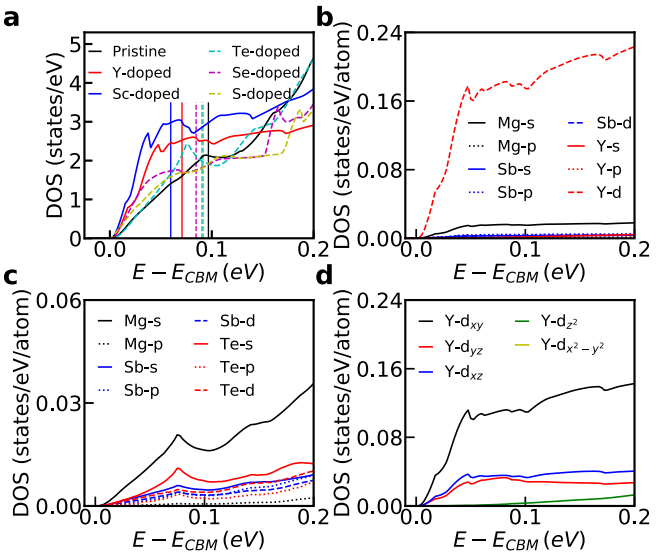

Fig. 3. a) Density of states of R-doped (R = Y, Sc, S, Se or Te) and pristine Mg_3Sb_2 supercells. The vertical lines represent the energy levels corresponding to a carrier concentration of -10^{20} cm^{-3}. The conduction band minimum (CBM) shifts to zero. **b and c)** Projected density of states per atom of Y-doped and Te-doped Mg_3Sb_2. **d)** The d-orbital projected density of states per atom of Y-doped Mg_3Sb_2.

increases near the bottom of the conduction band. Also, for the systems doped with the chalcogen group elements (i.e., S, Se or Te), the change of DOS near the CBM is less significantly. To clarify the effects of group-3 and chalcogen group elements doping, we calculated the projected density of states (PDOS) per atom of the representative Y-doped and Te-doped Mg_3Sb_2 (see Fig. 3**b)** and Fig. 3**c)**). Note that the DOS of Y-d states is dominantly larger than others, and a sharp increase of the DOS of Y-d states results in the overall increase of the total DOS. Furthermore, in Fig. 3**d)**, the d_{xy} orbital makes the major contribution to the Y-d PDOS near CBM. In contrast, after doping Te to the Sb lattice site, Mg-s states still dominate the DOS near CBM, and Te does not have a significant influence on the CBM.

Fig. 4 shows the unfolded effective band structures of Y-doped and Te-doped Mg_3Sb_2. Note that the band gaps of these effective

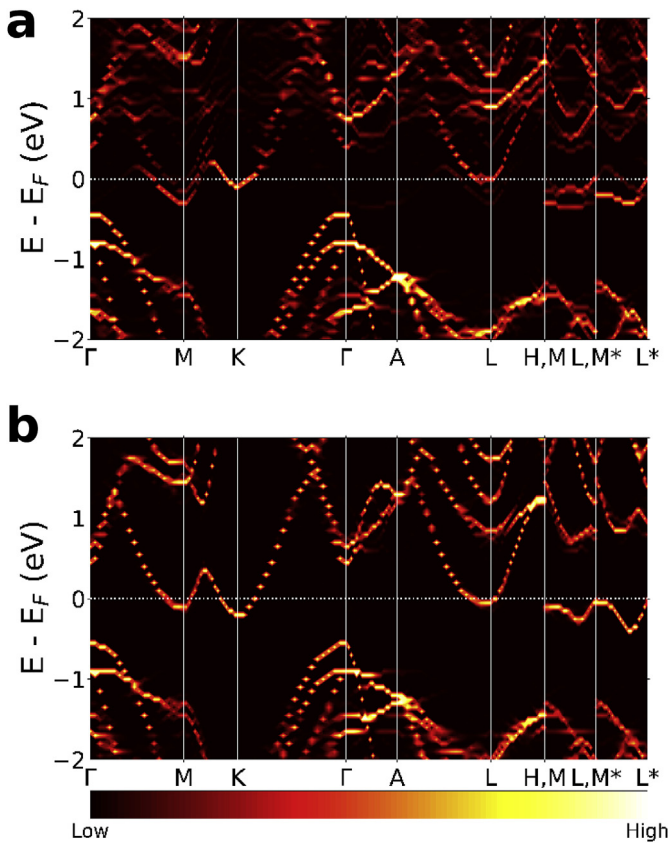

Fig. 4. Effective band structures of Y-doped (a) and Te-doped (b) Mg_3Sb_2 supercells. The Fermi level is located at 0 eV.

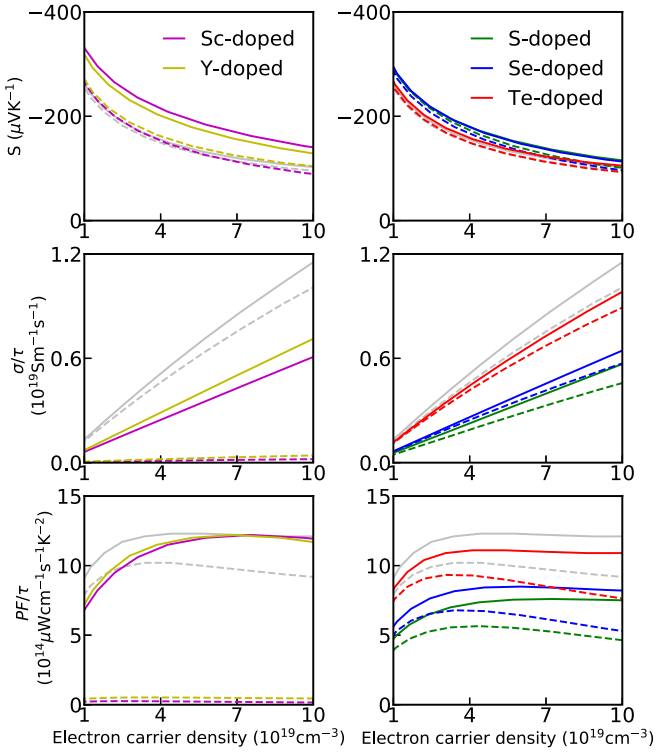

Fig. 5. The Seebeck coefficients (top), electrical conductivities normalized by the relaxation time (middle) and power factors normalized by the relaxation time (bottom) of doped and pristine Mg_3Sb_2 supercells at 300 K. In-plane and out-of-plane directions are represented by solid and dashed curves, respectively. The transport properties of pristine Mg_3Sb_2 (40-atom supercell) are denoted by gray curves as references.

band structures are underestimated due to the use of PBE functional. Compared to the band structure of pristine Mg_3Sb_2, relatively non-dispersive bands are formed in Y-doped Mg_3Sb_2 along M-L near the bottom of the conduction band. This is believed to be related to the large increase of DOS near the CBM. In addition, the electronic band at M point moves down and becomes very close to the conduction band minimum, promoting the band convergence. By comparison, the effective band structure of Te-doped Mg_3Sb_2 is similar to that of pristine Mg_3Sb_2 except that the Fermi level moves into the conduction bands due to the extra electrons.

We calculated the electrical transport properties along both the in-plane and out-of-plane directions of doped Mg_3Sb_2 supercells (see Fig. 5). The transport properties of pristine Mg_3Sb_2 (40-atom supercell) are also calculated and shown by gray curves in Fig. 5 as a reference. The electrical transport properties calculated with a 90-atom supercell are consistent with those of the 40-atom supercell, as shown in Fig. S5 in Supplemental Materials. Also, Sc-doped and Y-doped Mg_3Sb_2 are found to have larger Seebeck coefficients along the in-plane direction, which are consistent with their sharp increase of DOS near the CBM. From the analysis above, we found that the d_{xy} orbitals of Sc and Y play an important role in enhancing the Seebeck coefficient along the in-plane direction. In contrast, chalcogen group elements (S, Se and Te) do not improve the Seebeck coefficient. The Seebeck coefficient can be described by the Mott relation [44]:

$$S=\frac{\pi^2 k_B^2 T}{3q}\cdot\frac{d[ln(\sigma(E))]}{dE}|_{E=E_F}=\frac{\pi^2 k_B^2 T}{3q}\cdot\left[\frac{1}{n(E)}\frac{dn(E)}{dE}+\frac{1}{\mu(E)}\frac{d\mu(E)}{dE}\right]|_{E=E_F} \quad (3)$$

where k_B, $\sigma(E)$, $n(E)$ and $\mu(E)$ are the Boltzmann constant, energy-dependent electrical conductivity, carrier concentration and mobility, respectively. Because Sc and Y induce a distortion in DOS near CBM and increase the DOS effective mass and $\frac{dn(E)}{dE}$, they promote the enhancement of the Seebeck coefficient.

When a Sc or Y atom occupies the Mg1 lattice site, the normalized electrical conductivity along the out-of-plane direction decreases dramatically, resulting in a very low normalized power factor along this direction. The normalized power factors of Sc-doped and Y-doped Mg_3Sb_2 along the in-plane direction are greater than those of the chalcogen-doped systems. In the meantime, Te-doped Mg_3Sb_2 has a higher normalized electrical conductivity and normalized power factor than the S-doped and Se-doped systems. To clarify the effect of dopants on the electronic structure, the decomposed charge densities corresponding to the bottom of the conduction band of pristine Y-doped, and Te-doped Mg_3Sb_2 were calculated (see Fig. 6). The conduction electron distributions of Te-doped and pristine Mg_3Sb_2 are rather similar. However, Y is found to change the electron distribution near the CBM dramatically. After doping Y, most conduction electrons along the out-of-plane direction disappear, which is consistent with the very low normalized electrical conductivity along this direction.

4. Conclusions

We performed DFT calculations to investigate the effect of group-3 elements doping on the electronic structure and electrical transport properties of Mg_3Sb_2. Because n-type Mg_3Sb_2 had a higher thermoelectric performance rather than the p-type in experiment, we focused on the group-3 and chalcogen group doping elements (i.e., Sc, Y, S, Se and Te). The group-3 dopants were

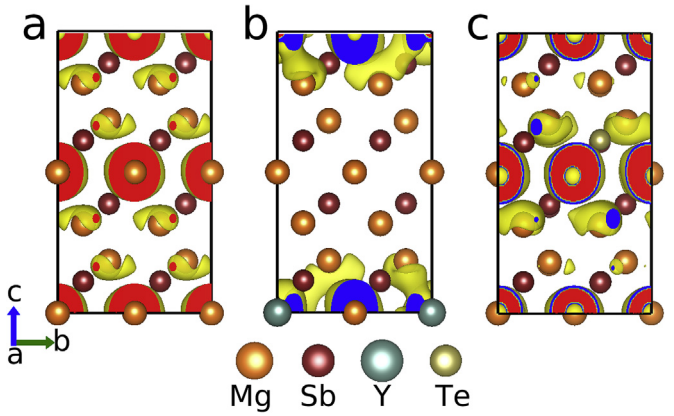

Fig. 6. Decomposed charge densities corresponding to the bottom of the conduction bands of pristine (a), Y-doped (b), and Te-doped (c) Mg_3Sb_2 supercells for a carrier concentration of -10^{20} cm^{-3}. The iso-surfaces correspond to a charge density of 5×10^{-5}e $bohr^{-3}$.

found to have a much stronger effect on the CBM of Mg_3Sb_2, compared to the chalcogen group elements. The increase of DOS effective mass induced by doping group-3 elements resulted in a higher Seebeck coefficient along the in-plane direction. Also, the group-3 elements led to a large suppression of the out-of-plane normalized electrical conductivity. For the chalcogen group elements, Te-doped Mg_3Sb_2 had a higher normalized power factor than the S-doped and Se-doped systems.

Declaration of competing interest

The authors declare that they have no known competing financial interests or personal relationships that could have appeared to influence the work reported in this paper.

Acknowledgements

This work was supported by the Research Grants Council of Hong Kong (17200017 and 17300018), the National Natural Science Foundation of China (51706192 and 11874313), the Zhejiang Provincial Natural Science Foundation (LR19A040001), and the Science, Technology and Innovation Commission of Shenzhen Municipality (JCYJ20180307154619840). The authors are grateful for the research computing facilities offered by ITS, HKU.

Appendix A. Supplementary data

Supplementary data to this article can be found online at https://doi.org/10.1016/j.jmat.2020.03.003.

References

[1] Jeng T-M, Tzeng S-C. Technical development of heat energy recovery for vehicle power system. Trans Can Soc Mech Eng 2013;37(3):885–94.
[2] Riffat SB, Ma X. Thermoelectrics: a review of present and potential applications. Appl Therm Eng 2003;23(8):913–35.
[3] Zhou D, Liu J, Xu S, Peng P. Thermal stability and elastic properties of Mg_3Sb_2 and Mg_3Bi_2 phases from first-principles calculations. Phys B Condens Matter 2010;405(13):2863–8.
[4] Liu H, Shi X, Xu F, Zhang L, Zhang W, Chen L, Li Q, Uher C, Day T, Snyder GJ. Copper ion liquid-like thermoelectrics. Nat Mater 2012;11(5):422.
[5] Martinez-Ripoll M, Haase A, Brauer G. The crystal structure of α-Mg_3Sb_2. Acta Crystallogr Sect B Struct Crystallogr Cryst Chem 1974;30(8):2006–9.
[6] Condron CL, Kauzlarich SM, Gascoin F, Snyder GJ. Thermoelectric properties and microstructure of Mg_3Sb_2. J Solid State Chem 2006;179(8):2252–7.
[7] Kim S, Kim C, Hong Y-K, Onimaru T, Suekuni K, Takabatake T, et al. Thermoelectric properties of Mn-doped Mg–Sb single crystals. J Mater Chem 2014;2(31):12311–6.
[8] Imasato K, Kang SD, Ohno S, Snyder GJ. Band engineering in Mg_3Sb_2 by alloying with Mg_3Bi_2 for enhanced thermoelectric performance. Mater. Horiz. 2018;5(1):59–64.
[9] Ohno S, Imasato K, Anand S, Tamaki H, Kang SD, Gorai P, et al. Phase boundary mapping to obtain n-type Mg_3Sb_2-based thermoelectrics. Joule 2018;2(1):141–54.
[10] Fu Y, Zhang X, Liu H, Tian J, Zhang J. Thermoelectric properties of Ag-doped compound: $Mg_{3-x}Ag_xSb_2$. J. Materiomics 2018;4(1):75–9.
[11] Zhang J, Song L, Pedersen SH, Yin H, Hung LT, Iversen BB. Discovery of high-performance low-cost n-type Mg_3Sb_2-based thermoelectric materials with multi-valley conduction bands. Nat Commun 2017;8:13901.
[12] Bjerg L, Madsen GK, Iversen BB. Ab initio calculations of intrinsic point defects in ZnSb. Chem Mater 2012;24(11):2111–6.
[13] Song L, Zhang J, Iversen BB. Simultaneous improvement of power factor and thermal conductivity via Ag doping in p-type Mg_3Sb_2 thermoelectric materials. J Mater Chem A 2017;5(10):4932–9.
[14] Shuai J, Wang Y, Kim HS, Liu Z, Sun J, Chen S, et al. Thermoelectric properties of Na-doped zintl compound: $Mg_{3-x}Na_xSb_2$. Acta Mater 2015;93:187–93.
[15] Tamaki H, Sato HK, Kanno T. Isotropic conduction network and defect chemistry in $Mg_{3+\delta}Sb_2$-based layered zintl compounds with high thermoelectric performance. Adv Mater 2016;28(46):10182–7.
[16] Zhang J, Song L, Mamakhel A, Jørgensen MRV, Iversen BB. High-performance low-cost n-type Se-doped Mg_3Sb_2-based zintl compounds for thermoelectric application. Chem Mater 2017;29(12):5371–83.
[17] Mao J, Zhu H, Ding Z, Liu Z, Gamage GA, Chen G, et al. High thermoelectric cooling performance of n-type Mg_3Bi_2-based materials. Science 2019;365(6452):495–8.
[18] Song S, Mao J, Bordelon M, He R, Wang Y, Shuai J, et al. Joint effect of magnesium and yttrium on enhancing thermoelectric properties of n-type zintl $Mg_{3+\delta}Y_{0.02}Sb_{1.5}Bi_{0.5}$. Mater. Today Phys. 2019;8:25–33.
[19] Shi X, Sun C, Zhang X, Chen Z, Lin S, Li W, et al. Efficient Sc-doped $Mg_{3.05-x}Sc_xSbBi$ thermoelectrics near room temperature. Chem Mater 2019;31(21):8987–94.
[20] Shi X, Zhao T, Zhang X, Sun C, Chen Z, Lin S, et al. Extraordinary n-type Mg_3SbBi thermoelectrics enabled by yttrium doping. Adv Mater 2019;31(36):1903387.
[21] Gorai P, Ortiz BR, Toberer ES, Stevanović V. Investigation of n-type doping strategies for Mg_3Sb_2. J Mater Chem 2018;6(28):13806–15.
[22] Gorai P, Toberer ES, Stevanović V. Effective n-type doping of Mg_3Sb_2 with group-3 elements. J Appl Phys 2019;125(2):025105.
[23] Shen J, Chen Y. Silicon as an unexpected n-type dopant in BiCuSeO thermoelectrics. ACS Appl Mater Interfaces 2017;9(33):27372–6.
[24] Zhang Q, Cao F, Liu W, Lukas K, Yu B, Chen S, et al. Heavy doping and band engineering by potassium to improve the thermoelectric figure of merit in p-type PbTe, PbSe, and $PbTe_{1-y}Se_y$. J Am Chem Soc 2012;134(24):10031–8.
[25] Yu H, Shaikh AR, Xiong F, Chen Y. Enhanced out-of-plane electrical transport in n-type SnSe thermoelectrics induced by resonant states and charge delocalization. ACS Appl Mater Interfaces 2018;10(12):9889–93.
[26] Cui J, Chen C, He W, Avila J, Zhao L-D, Asensio MC, et al. Large enhancement of electrical transport properties of SnS in the out-of-plane direction by n-type doping: a combined ARPES and DFT study. J Mater Chem 2018;6(47):24588–94.
[27] Hohenberg P, Kohn W. Inhomogeneous electron gas. Phys Rev 1964;136(3B):B864.
[28] Kohn W, Sham LJ. Self-consistent equations including exchange and correlation effects. Phys Rev 1965;140(4A):A1133.
[29] Payne MC, Teter MP, Allan DC, Arias T, Joannopoulos aJ. Iterative minimization techniques for ab initio total-energy calculations: molecular dynamics and conjugate gradients. Rev Mod Phys 1992;64(4):1045.
[30] Kresse G, Furthmüller J. Efficient iterative schemes for ab initio total-energy calculations using a plane-wave basis set. Phys Rev B 1996;54(16):11169.
[31] Medeiros PV, Stafström S, Björk J. Effects of extrinsic and intrinsic perturbations on the electronic structure of graphene: retaining an effective primitive cell band structure by band unfolding. Phys Rev B 2014;89(4):041407.
[32] Perdew JP, Burke K, Ernzerhof M. Generalized gradient approximation made simple. Phys Rev Lett 1996;77:3865–8.
[33] Tran F, Blaha P. Accurate band gaps of semiconductors and insulators with a semilocal exchange-correlation potential. Phys Rev Lett 2009;102(22):226401.
[34] Madsen GKH, Carrete J, Verstraete MJ. BoltzTraP2, a program for interpolating band structures and calculating semi-classical transport coefficients. Comput Phys Commun 2018;231:140–5.
[35] Giannozzi P, Baroni S, Bonini N, Calandra M, Car R, Cavazzoni C, et al. Quantum espresso: a modular and open-source software project for quantum simulations of materials. J Phys Condens Matter 2009;21(39):395502.
[36] Poncé S, Margine ER, Verdi C, Giustino F. EPW: electron–phonon coupling, transport and superconducting properties using maximally localized wannier functions. Comput Phys Commun 2016;209:116–33.
[37] Goedecker S, Teter M, Hutter J. Separable dual-space Gaussian pseudopotentials. Phys Rev B 1996;54(3):1703.
[38] Hartwigsen C, Gœdecker S, Hutter J. Relativistic separable dual-space Gaussian pseudopotentials from H to Rn. Phys Rev B 1998;58(7):3641.
[39] Askarpour V, Maassen J. Unusual thermoelectric transport anisotropy in quasi-two-dimensional rhombohedral GeTe. Phys Rev B 2019;100(7):075201.
[40] Ponnambalam V, Morelli DT. On the thermoelectric properties of zintl

compounds $Mg_3Bi_{2-x}Pn_x$ (Pn= P and Sb). J Electron Mater 2013;42(7):1307–12.
[41] Mao J, Wu Y, Song S, Zhu Q, Shuai J, Liu Z, et al. Defect engineering for realizing high thermoelectric performance in n-type Mg_3Sb_2-based materials. ACS Energy Lett. 2017;2(10):2245–50.
[43] Chen X, Wu H, Cui J, Xiao Y, Zhang Y, He J, et al. Extraordinary thermoelectric performance in n-type manganese doped Mg_3Sb_2 zintl: high band degeneracy, tuned carrier scattering mechanism and hierarchical microstructure. Nano Energy 2018;52:246–55.
[44] Cutler M, Mott NF. Observation of anderson localization in an electron gas. Phys Rev 1969;181(3):1336.

Yue Chen is an assistant professor at the University of Hong Kong, Department of Mechanical Engineering. His research interests focus on the materials physics for electrical and thermal transports, such as electronic structures and lattice dynamics. His interests stem from the studies of materials science at Oxford University and Beihang University. He was a postdoctoral fellow at Columbia University in the City of New York and Institute of Metal Research, Chinese Academy of Sciences before joining HKU.